

## Article

# Quantifying the Effects of Grain Refiners Al-Ti-B and La on the Microstructure and Mechanical Properties of W319 Alloy

Xinxu Liu <sup>1</sup>, Bing Wang <sup>1</sup>, Quan Li <sup>1</sup>, Junsheng Wang <sup>1,2,\*</sup> , Chi Zhang <sup>1</sup>, Chengpeng Xue <sup>1</sup>, Xinghai Yang <sup>1</sup>, Guangyuan Tian <sup>1</sup>, Xiaoguang Liu <sup>3,\*</sup> and Hongqun Tang <sup>4,\*</sup> 

<sup>1</sup> School of Materials Science & Engineering, Beijing Institute of Technology, Beijing 100081, China; 3220201165@bit.edu.cn (X.L.); 3120191176@bit.edu.cn (B.W.); 3220215174@bit.edu.cn (Q.L.); 3120185587@bit.edu.cn (C.Z.); 3120195590@bit.edu.cn (C.X.); 3220205159@bit.edu.cn (X.Y.); 3120205545@bit.edu.cn (G.T.)

<sup>2</sup> Advanced Research Institute of Multidisciplinary Science, Beijing Institute of Technology, Beijing 100081, China

<sup>3</sup> School of Materials Science and Engineering, University of Science & Technology Beijing, Beijing 100083, China

<sup>4</sup> Guangxi Key Laboratory of Processing for Nonferrous Metals and Featured Materials, Center of Ecological Collaborative Innovation for Aluminium Industry in Guangxi, School of Resources, Environment and Materials, Guangxi University, Nanning 530004, China

\* Correspondence: junsheng.wang@bit.edu.cn (J.W.); liuxg@ustb.edu.cn (X.L.); hqtang@gxu.edu.cn (H.T.)

**Abstract:** It is well known that the microstructure distribution in recycled Al-Si alloys has a large impact on the final mechanical properties. In this study, the microstructure, including Fe-rich intermetallics and microporosity, was quantitatively adjusted using multi-scale characterization with microalloying rare earth elements and traditional grain refiners as the objects of study. It was found that the addition of Al-Ti-B to W319 recycled aluminum alloy reduces the microstructure size and Fe-rich intermetallics, while the addition of La facilitates the transformation of harmful  $\beta$ -Fe into less harmful particles and the densification of coarse eutectic Si, promoting the refining effects on the microstructure additionally. Therefore, the RE and Al-Ti-B master alloy could be a potential new grain refining agent, especially for Al-cast alloys when the ductility is critical for designing. The improvement in elongation far exceeds the original level, up to 69.6%, while maintaining the same level of strength or even better. At the same time, the excessive addition of La may lead to the depletion of Cu and Ti elements during heat treatment, degrading ductility and strength.

**Keywords:** aluminum alloy; Al-Ti-B; La; microporosity; X-ray computed tomography (XCT); U-net CNN



**Citation:** Liu, X.; Wang, B.; Li, Q.; Wang, J.; Zhang, C.; Xue, C.; Yang, X.; Tian, G.; Liu, X.; Tang, H. Quantifying the Effects of Grain Refiners Al-Ti-B and La on the Microstructure and Mechanical Properties of W319 Alloy. *Metals* **2022**, *12*, 627. <https://doi.org/10.3390/met12040627>

Academic Editor: Talal Al-Samman

Received: 25 February 2022

Accepted: 1 April 2022

Published: 5 April 2022

**Publisher's Note:** MDPI stays neutral with regard to jurisdictional claims in published maps and institutional affiliations.



**Copyright:** © 2022 by the authors. Licensee MDPI, Basel, Switzerland. This article is an open access article distributed under the terms and conditions of the Creative Commons Attribution (CC BY) license (<https://creativecommons.org/licenses/by/4.0/>).

## 1. Introduction

With the advantages of low density, high specific strength, good corrosion resistance and recyclability, aluminum alloys are widely used in automotive, aerospace and other fields. However, the high energy consumption and carbon emissions of the aluminum electrolysis process restrict the further development of the industry. For the core technology problem of “low carbon aluminum”, recycled cast aluminum alloy technology reduces carbon emission by more than 95% and has good development prospects. The rapid development of modern industry has brought about a further increase in the demand for the comprehensive mechanical properties of materials. For recycled cast Al-Si alloys, it is crucial to precisely reveal the fine structural characteristics of the alloys and quantitatively correlate them with the mechanical properties in order to meet the more demanding requirements of social development [1–3].

It is well known that grain refinement is the most effective way to simultaneously improve both strength and plasticity. For current industrial production, researchers spent a lot of time exploring microstructure refinement methods and their mechanisms of action,

among which the addition of the representative grain refiner Al-5Ti-1B can significantly improve the performance of the material [4–7]. However, grain refiners have very limited effects on other defects, such as the second phase and microporosity. Therefore, it is imperative to find an effective method to fully modulate the organization and properties of Al-Si alloys on this basis. Previous studies showed that, similar to refiners, rare earth(RE)elements also have the effect of refining microstructure; the refining effect and mechanism of different RE elements are not exactly the same [8–11]. Colombo et al. [12] found that secondary dendrite arm spacing (SDAS) was only related to alloy composition when casting conditions were constant, and the primary Al<sub>3</sub>Er precipitation from the melt could act as a nucleating agent for  $\alpha$ -Al dendrites, reducing SDAS by 27.8%. Zhang [13] showed that Sc could promote the nucleation of  $\alpha$ -Al grains and Al<sub>2</sub>Cu precipitates, resulting in the reduction of Al-Cu alloy grain size from 163.5  $\mu\text{m}$  to 61.5  $\mu\text{m}$ , which is a very effective refining agent. In addition to direct effects on grain size and SDAS, the Yb-rich dispersed phase in aluminum alloys is reported to inhibit the recrystallization ability of the aluminum matrix and retain reversible deformability [14]. Compared with most RE elements, La has good refinement ability, and the content of La in the crust is much richer than that of Sc, Yb, Er and so on. It is reported that 0.06  $\mu\text{m}$  wt.% La can achieve the ideal effect of microstructure refinement, and the degree of grain refinement is 48.4% [15].

In addition, RE also has a positive metamorphic effect on the second phase of the Al-Si alloys, and the effect is not identical depending on the type of element [16,17]. Nogita et al. [18] compared the effect of various RE elements (Ce, Eu, Er, Yb, etc.) on the densification of eutectic Si and found that all of them were able to reduce the nucleation temperature and transform the morphology with Eu having the most complete densification effect. Moreover, the continuous enrichment of Fe elements during the casting of aluminum alloys leads to the formation of needle-like Fe-rich intermetallics, which seriously affects the mechanical properties of the material. In this regard, attention is focused on the mechanism of Fe-rich phase formation and the search for ways to reduce its hazard [19,20]. In addition to the addition of well-known neutralizing elements, such as Mn, Cr, etc. [21], the effect and mechanism of RE elements on Fe metamorphism are also investigated. Shi et al. [22] found that Er can break and refine the needle-like  $\beta$ -AlFeSi phase and reduce the hazard of needle-like  $\beta$ -AlFeSi relative to its' alloy properties, in addition to refining  $\alpha$ -Al grains and metastable eutectic Si organization in A356 aluminum alloys. Li et al. [23] found that the amount of needle-like  $\beta$ -AlFeSi phase was reduced and replaced by the formation of  $\alpha$ -AlFeSiRE phase after the addition of mixed RE to the Al-10Si-3Cu alloy.

Further, the Fe-rich phase not only directly increases the occurrence of stress concentrations but also promotes the formation of micropores, another common defect. This is due to the formation of lamellar  $\beta$ -Fe between the dendrites during solidification, which impedes the flow of the aluminum solution and causes difficulty in filling the shrinkage, leading to the formation of micropores [24,25]. As a key factor affecting the casting performance, especially the elongation, many recent explorations on porosity focused on the addition of alloying elements and the control of the cooling rate [26,27], and fewer studies were conducted on the effect of RE elements on microporosities.

To sum up, it is not enough to rely on the refining effect of Al-Ti-B on  $\alpha$ -Al alone to improve the performance; we need to add RE elements to facilitate overall control concerning several other common defects in castings. Although much work is conducted on the effects of grain refiners or RE elements on alloy properties, there is a lack of sufficient systematic studies on the advantages and mechanisms of action of the composite addition of both. In this paper, we will quantitatively elucidate the effect of La/Al-Ti-B on the distribution characteristics of the second phase and defects. By simultaneously adding Al-Ti-B and different contents of La elements, this paper explores the synergistic mechanism of the two elements and provides a multi-scale quantitative description of the microstructure control results of castings, which provides an effective new idea for improving the performance of recycled cast aluminum alloys.

## 2. Materials and Methods

### 2.1. Thermodynamic Simulation

For the study of the synergistic regulation of the organization and properties of the present alloy system by the grain refiners and La, we used Pandat thermodynamic calculation software (CompuTherm LLC, Middleton, WI, USA) to first determine the alloy composition and the additional amounts. The effect of the additional amounts of La and Fe on the phase composition of the alloy at equilibrium was calculated, as shown in Figure 1a. The results indicate that the La/Fe value affects the type of Fe-rich intermetallics to some extent. When the Fe content is high, two types of Fe-rich intermetallics,  $\alpha$ -Fe and  $\beta$ -Fe, will appear. According to previous experience,  $\beta$ -Fe has a serious cutting effect on the substrate due to its needle-like morphology, which severely reduces the mechanical properties, including elongation. To deal with this phenomenon, an effective way is to promote the conversion of  $\beta$ -Fe to  $\alpha$ -Fe; as the Fe content decreases,  $\beta$ -Fe disappears. When the Fe content decreases further, the effective Fe neutralizing element, Mn, becomes excessive and generates  $\text{Al}_{12}\text{Mn}$ , which is not a good phenomenon for the alloy properties. When the La/Fe ratio is  $>2.5$ , the RE element excess appears as a La-rich phase. Therefore, in order to investigate the regulation law of La in the second phase, including the Fe-rich phase, it was decided to set the additions of La at 0.05%, 0.1% and 0.3% by mass percentage, respectively.

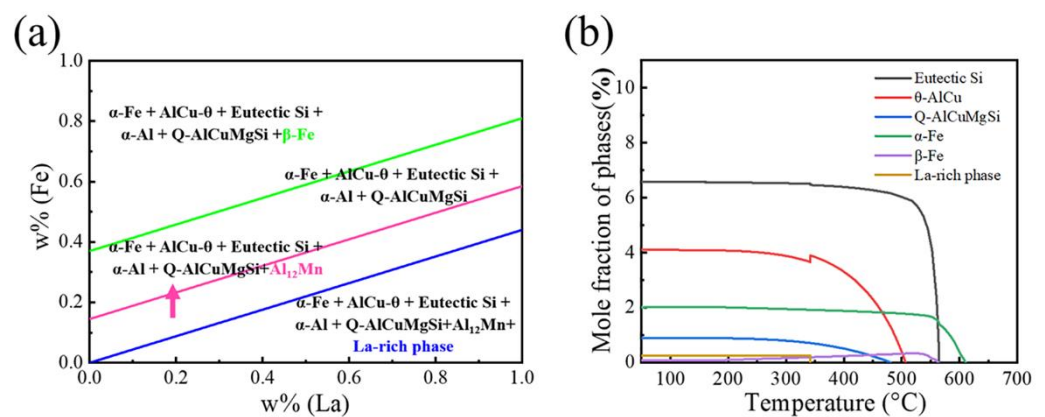


**Figure 1.** (a) Effect of Fe/La content on intermetallic compounds in W319 alloy at room temperature; (b) Phase fraction as a function of temperature at equilibrium for the W319 + 0.1La alloy system.

In addition, we calculated the equilibrium phase diagram of  $\text{Al-7.3Si-3.5Cu-0.3Mg-0.4Fe-0.3Mn-0.03Ti-0.1La}$  at room temperature that was used to guide the subsequent experiments and discussions. As shown in Figure 1b, the alloy system used mainly consists of eutectic Si,  $\text{AlCu-}\theta(\text{Al}_2\text{Cu})$ , Q-phase and two Fe-rich intermetallics,  $\alpha$ -Fe( $\text{AlFeMnSi}$ ) and  $\beta$ -Fe( $\text{AlFeSi}$ ), where  $\alpha$ -Fe accounts for about 2% (in molar %) of the alloy phase composition, while the total amount of  $\beta$ -Fe starts to precipitate at  $570^\circ\text{C}$ , reaching up to about 0.2% then gradually decreases; the addition of La generates the RE-rich phase. As can be seen from the figure, the generation of the La-rich phase corresponds to the reduction of  $\text{Al}_2\text{Cu}$ , which is an important strengthening phase, and it is reasonable to speculate that this phenomenon may be detrimental to the material strength.

### 2.2. Sample Preparation

In this paper, six compositions were designed for experimental investigation. #1, called base, is an  $\text{Al-7.3Si-3.5Cu-0.3Mg-0.4Fe-0.3Mn}$  alloy system; #2 with only 0.6 wt.% Al-Ti-B added is called AlTiB; #3 with only 0.1 wt.% La added is called 0.1La; #4, #5 and #6 are all compounded with La and 0.6 wt.% Al-Ti-B; the additions of La are 0.05 wt.%, 0.1 wt.% and 0.3 wt.%, corresponding to the three groups called AlTiB + 0.05La, AlTiB + 0.1La and AlTiB + 0.3La, respectively. The above 6 groups of experimental alloys were prepared from pure Al, Al-20Si, Al-50Cu, Al-20Mg, Al-20Fe, Al-20Mn, Al-10La and Al-5Ti-1B. The

chemical composition of the 6 groups of alloys was detected using the X-ray fluorescence spectrometer (XRF-1800) produced by Shimadzu Corporation, Kawaguchi, Japan, and the results are presented in Table 1.

**Table 1.** Chemical compositions of the aluminum alloys (wt.%).

Alloys	Al	Si	Cu	Fe	Mg	Mn	Ti	La
Base	89.13	7.18	3.56	0.44	0.29	0.30	-	-
AlTiB	89.45	7.12	3.39	0.44	0.28	0.30	0.03	-
0.1La	89.20	7.10	3.48	0.43	0.29	0.29	-	0.11
AlTiB + 0.05La	89.25	7.20	3.38	0.42	0.26	0.31	0.03	0.06
AlTiB + 0.1La	89.14	7.15	3.49	0.43	0.28	0.30	0.03	0.09
AlTiB + 0.3La	88.81	7.20	3.55	0.42	0.29	0.30	0.03	0.31

All raw materials were polished and shaken with alcohol. The raw materials were preheated in a heat treatment furnace oven (Kejing Material Technology Co., Ltd., Hefei, China) at 200 °C for 30 min before casting, and then the preheated raw materials were heated in a graphite crucible until melted and held at 730 °C for 20 min. The aluminum solution was subsequently poured into a copper mold, and the castings were removed after cooling. The final casting size was 170 mm × 50 mm × 23 mm, and the sampling locations required for the experiments are shown in Figure 2a. The shape and size of the tensile specimen are shown in Figure 2b. The maximum length and width are 65 mm and 10 mm, respectively; the thickness is 2 mm. The metallographic specimens' size is 10 mm × 10 mm × 7 mm. The X-ray computed tomography (XCT) cylindrical specimens are  $\Phi$ 1.6 mm in diameter and greater than 40 mm in length. Six alloy samples were quenched in water immediately after double-stage solid solution at 450 °C—4 h + 500 °C—8 h to obtain a uniform supersaturated solid solution. Subsequently, the alloy was aged at 180 °C for 7 h, at which time the microhardness reached its maximum.

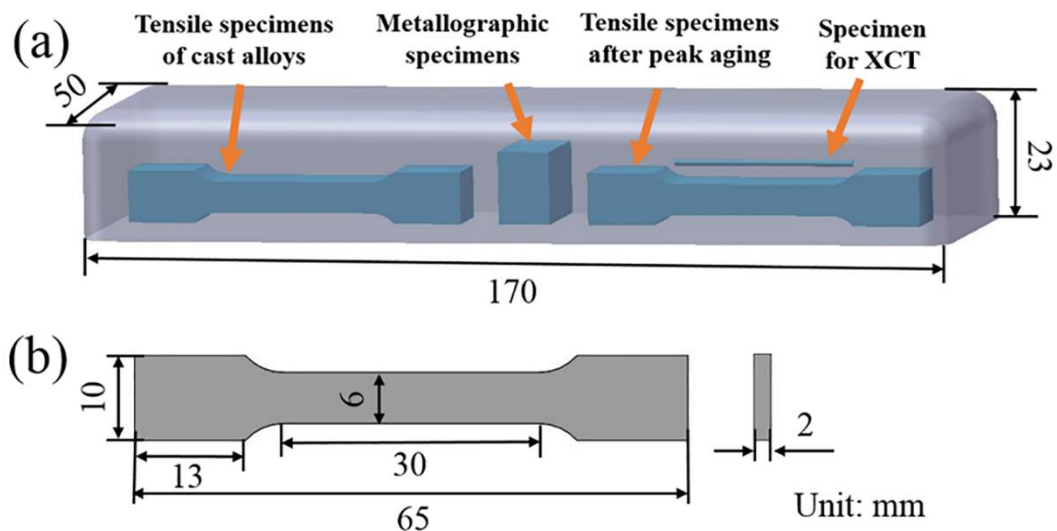


**Figure 2.** (a) Casting size and sampling location; (b) Tensile specimen shape and size.

### 2.3. Characterization and Analysis Methods

According to standard procedures, the samples were polished with 800~2000# SiC sandpaper, followed by a 3.5  $\mu$ m and 1.0  $\mu$ m diamond paste as well as a colloidal silica suspension. The samples were subsequently etched with Keller's reagent (95% H<sub>2</sub>O, 2.5% HNO<sub>3</sub>, 1.5% HCl and 1.0% HF). The LWD200-4XC Optical Microscope (OM, Shanghai Tiewei Optoelectronics Technology Co., Shanghai, China.) was used to observe samples before and after etching to quantify eutectic Si and SDAS. Before etching, 8 metallographic

images of each sample were selected for extracting and quantifying eutectic Si. Traditional threshold segmentation methods are not satisfactory enough in terms of detail, so this paper chooses to replace them with Dragonfly's feature extraction U-net CNN machine learning algorithm, which outputs the data of the samples based on the grayscale, morphology and location information of the input model. The extraction results converted to binary images were imported into ImageJ (ImageJ 1.8.0.172, National Institutes of Health(NIH), Stapleton, NY, USA) to analyze the size and morphological information of all eutectic Si particles. The SDAS was measured by the truncation method after corrosion, in which 6 photographs were selected for each sample, and 5 SDAS were counted for each image. The microstructures of polished samples were characterized using a Hitachi S4800 Field Emission Scanning Electron Microscope (FE-SEM, Tokyo, Japan) coupled with energy dispersive X-ray spectroscopy (EDS).

In order to obtain the 3D characteristics of the micropores and Fe-rich intermetallics, cylindrical specimens were scanned using high-resolution phase-contrast X-ray computed tomography (XCT) from Xradia 520 Versa of ZEISS (Carl Zeiss Microscopy GmbH, Jena, Germany). In this experiment, the XCT volume scans were performed at an accelerating voltage of 60 kV and a target power of 5 W. A total of 997 images with 180° rotation were acquired, which were then constructed into 3D volume with a voxel size of  $1.2 \mu\text{m} \times 1.2 \mu\text{m} \times 1.2 \mu\text{m}$ . The gray projection image with structural information was obtained based on the different absorption of X-rays by the internal structure of the alloy, which can be used to extract microstructure. Due to the inhomogeneous brightness and blurred boundaries of the XCT 2D reconstructed slice images, we again used the machine learning algorithm to extract eutectic Si and Fe-rich intermetallics and micropores from the 3D XCT data and then performed volume rendering to obtain feature quantification by Avizo [28,29].

The alloy specimens were subjected to the necessary hardness and tensile tests to investigate the effect of Al-Ti-B and La on the mechanical properties of the alloy and to find its connection with microstructural changes. Microhardness tests were performed using a digital microhardness tester (TMVS-1, Beijing Times Zhongyi Technology Co., Ltd. Beijing, China) with a set load of 200 gf and a duration of 10 s. The tests were repeated 10 times for each sample. Tensile tests were performed at room temperature using a SUNS UTM6104 electronic universal tensile machine (Sansi Technology Co., Ltd., Shenzhen, China) to obtain yield strength, strength and elongation (strain rate of 1 mm/min), where elongation was measured manually using vernier calipers.

### 3. Results

#### 3.1. As-Cast Microstructure Characteristics

##### 3.1.1. Quantitative and Statistical SDAS

In this paper, extensive characterization of the microstructure was performed. Etched samples were used to count the secondary dendrite arm spacing. Similar to grain size (GS), SDAS is also a function of cooling rate and follows a similar pattern. Metals with fast cooling rates, high nucleation temperatures and good subcooling of the crystallization process always have high dendrite nucleation rates. If there is not enough time to complete the growth and aggregation process, the SDAS is smaller and is accompanied by causing a significant increase in the tensile strength, yield strength and plasticity of the alloy. Moreover, Ghassemali et al. argue that SDAS is a more dominant factor than GS in influencing the mechanical properties of the alloy [30,31].

Figure 3 show the quantitative and statistical results of the microscopic morphology and SDAS of the six groups of samples. As shown in the figure, the SDAS of base was the largest with an average of  $21.1 \pm 2.2 \mu\text{m}$ , and the addition of 0.6 wt.% Al-Ti-B and 0.1 wt.% La significantly reduced the SDAS values with statistical results of  $16.5 \pm 1.6 \mu\text{m}$  and  $15.0 \pm 1.2 \mu\text{m}$ , respectively, which were 22.0% and 29.2% lower compared with base. The combination of La and Al-Ti-B brought more effective refinement, and the overall reduction of SDAS was positively correlated with the amount of La added. Among

them, AlTiB + 0.3La had the smallest SDAS among the six alloy samples with a value of  $12.7 \pm 1.4 \mu\text{m}$ , which is 39.8% lower than that of base.

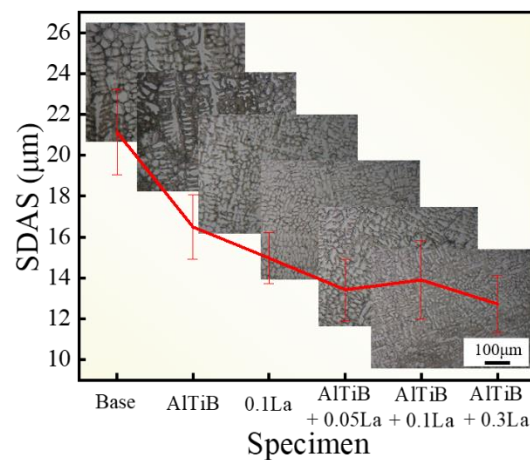


**Figure 3.** Metallographic morphology and SDAS statistics of 6 groups of alloys after corrosion.

La has strong surface activity, and the addition of La can reduce the surface tension of the aluminum solution and make the wetting angle decrease. According to the classical heterogeneous nucleation theory, the crystal billets can reach the critical radius at a small degree of subcooling, thus improving the nucleation ability of  $\alpha$ -Al. Meanwhile, due to the negligible solubility of La in  $\alpha$ -Al, most of the La will be enriched at the interface between  $\alpha$ -Al and the liquid phase, causing a constitutional supercooling that limits grain growth, which is responsible for the microstructure refinement caused by the addition of the element La [32,33].

### 3.1.2. Morphology and Size Statistics of Eutectic Si

The addition of 7.3 wt.% Si enhances the casting properties of the alloy, but on the other hand, the excess Si element deteriorates the alloy properties by forming coarse slab-like eutectic Si. This is due to the presence of internal defects in the eutectic Si, which does not grow uniformly in all directions at the same rate, but grows selectively.

As shown below, Figure 4a–f show the brightness-unified images of the six alloy samples. We extracted eutectic Si as binarized data and then performed quantitative statistics. The size variation pattern was expressed in terms of the average equivalent diameter, showing the distribution of the number of eutectic Si particles in different size ranges, and the results are displayed in Figure 4g. The morphological features were measured by two criteria: roundness and aspect ratio, as shown in Figure 4h.

Observing Figure 4g,h, it is logical that base has the largest Si-phase mean equivalent diameter, the smallest roundness and the largest aspect ratio of  $3.35 \pm 0.97 \mu\text{m}$ ,  $0.37 \pm 0.09$  and  $1.98 \pm 0.28$ , respectively. The addition of Al-Ti-B limits the growth of eutectic Si distributed at grain boundaries due to grain refinement, resulting in a slight reduction in the size and the number of long Si phases that bring negative effects, which is reflected in the numerical changes in aspect ratio and roundness. The addition of 0.1 wt.% La leads to a transformation of the Si phase from coarse slabs to fibrous and granular; numerically, the average equivalent diameter of 0.1 La decreases by 25.7%, roundness increases by 18.9% and aspect ratio decreases by 16.2% relative to base, which can be observed to be mainly due to the fragmentation of coarse eutectic Si. When comparing 0.1La and AlTiB, it is found that 0.1La has a more significant effect on the metamorphism of eutectic Si. It is worth noting that the same conclusion can be drawn by comparing 0.1La and AlTiB + 0.05La samples, where the additional 0.05 wt.% La caused more intense metamorphism. The composite addition can superimpose the effect of both on the optimization of the organization and the metamorphic ability of eutectic Si increases with the increase of La addition. The equivalent

diameter, roundness and aspect ratio of AlTiB + 0.3La that achieved the best metamorphic effect were  $2.37 \pm 0.47 \mu\text{m}$ ,  $0.48 \pm 0.05$  and  $1.58 \pm 0.25$ , respectively, achieving favorable changes of 29.3%, 29.7% and 20.2% compared to base.

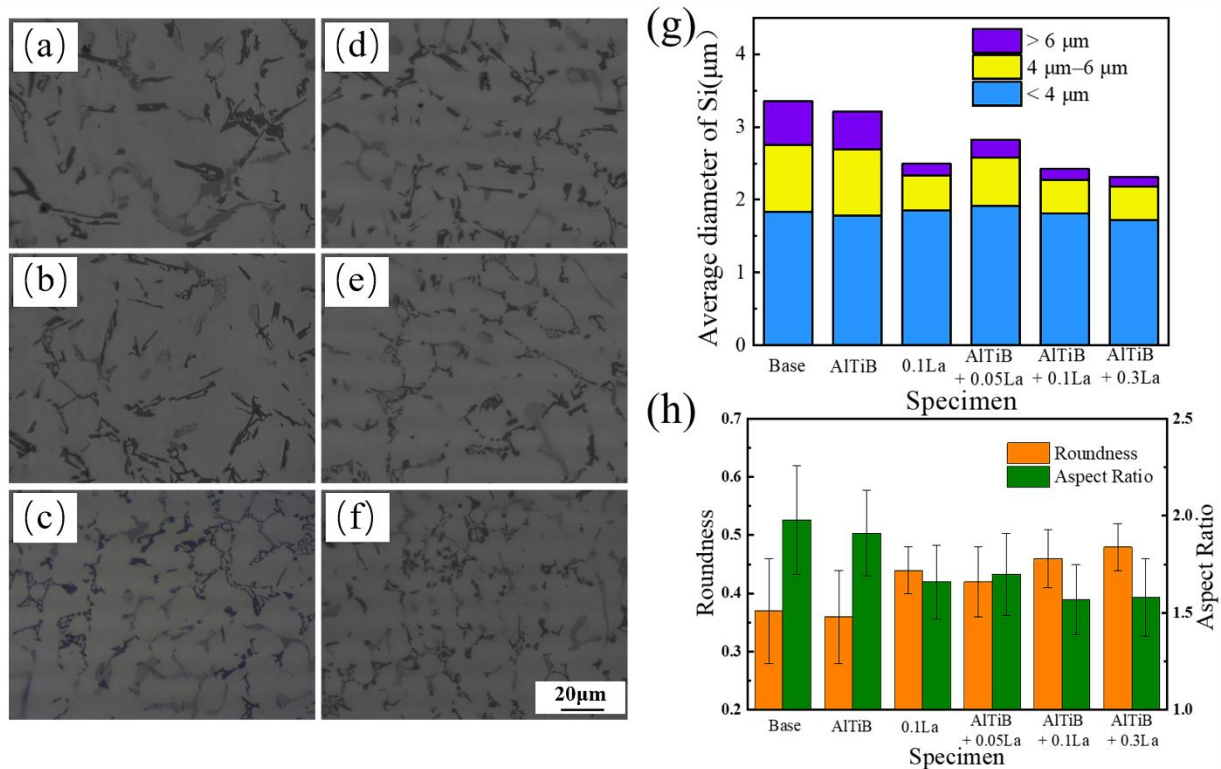


**Figure 4.** Optical microstructure and morphological characteristics statistics of eutectic Si particles: (a) Base; (b) AlTiB; (c) 0.1La; (d) AlTiB + 0.05La; (e) AlTiB + 0.1La; (f) AlTiB + 0.3La; (g) Average equivalent diameter and number distribution of different sizes; (h) Roundness and aspect ratio statistics.

The metamorphic effect of La on eutectic Si originates from the many fine, diffusely-distributed RE elements, where La atoms accumulate in concave valleys, causing lattice distortion and reducing the growth rate of eutectic Si in that direction while changing the original growth pattern of eutectic Si, resulting in the refinement of the eutectic Si from initially massive or needle-like to fibrous or granular [34–36].

### 3.1.3. Two-Dimensional observation of As-Cast Intermetallics

Figure 5 show the microstructure morphology and the SEM/EDS surface scan results of the as-cast Al-Si alloys in localized areas; the corresponding point scans for different intermetallic compounds are shown in Table 2. Based on the thermodynamic simulation analysis, the type of Fe-rich intermetallic can be determined by the presence or absence of Mn elements. If the enrichment of Mn elements is also present in the Fe-rich region, it is considered as  $\alpha$ -Fe, otherwise  $\beta$ -Fe.

In base, obvious needle-like Fe-rich intermetallics were observed, which were detected as  $\beta$ -Fe by EDS; observation of AlTiB + 0.05La revealed a significant decrease in needle-like  $\beta$ -Fe and an increase in the number of skeleton-like Fe-rich intermetallics. The results of the point scan and surface scan show the coexistence of Mn and Fe, so it can be judged as  $\alpha$ -Fe. Additionally, the enrichment of La elements around Fe compounds was found in the local magnification and surface scan results. Due to the strong interaction between Fe and La, some Fe in the  $\beta$ -AlFeSi phase will be replaced by RE elements to form stable  $\alpha$ -Fe, which confirms the effectiveness of La in promoting the transformation of  $\beta$ -Fe to  $\alpha$ -Fe and is consistent with the thermodynamic calculations.

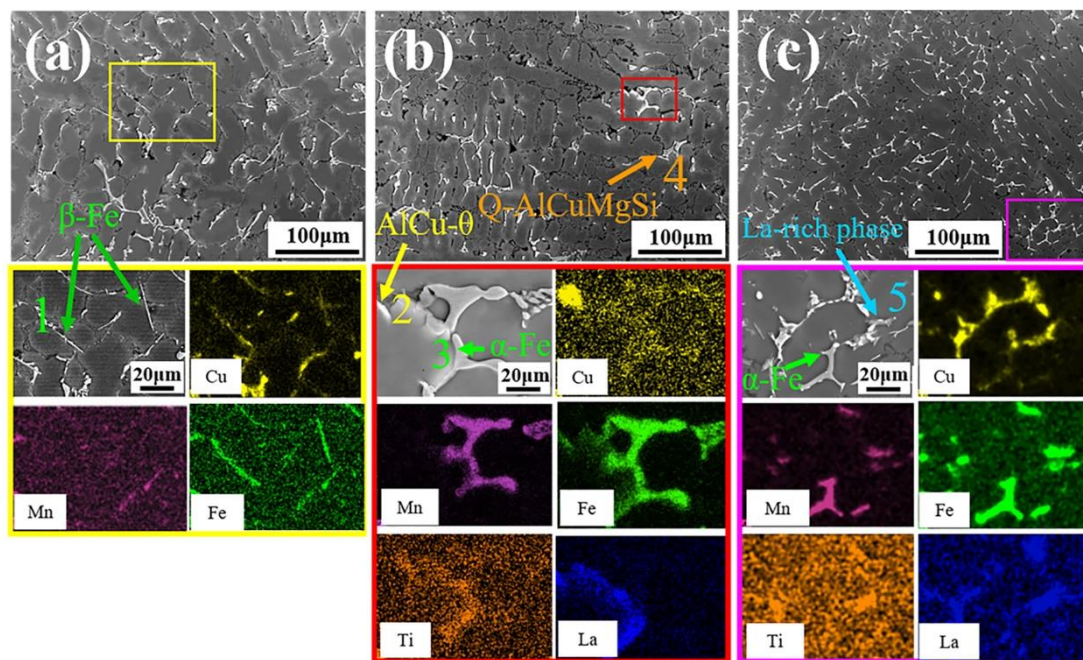


**Figure 5.** As-cast SEM/EDS micrographs of the (a) Base; (b) AlTiB + 0.05La; (c) AlTiB + 0.3La. The different colors of numbers are meant to correspond to different elements in the EDS image.

**Table 2.** Composition of intermetallic phases (at.%) in as-cast alloy.

Number	Al	Si	Cu	Mg	Fe	Mn	La	Intermetallic
1	93.08	1.75	3.99	-	1.18	-	-	$\beta$ -Fe
2	94.36	-	5.64	-	-	-	-	AlCu- $\theta$
3	80.60	8.05	2.06	-	5.25	4.04	-	$\alpha$ -Fe
4	91.41	3.79	1.76	3.04	-	-	-	Q-AlCuMgSi
5	88.01	2.86	7.67	-	-	-	1.46	La-rich phase

In AlTiB + 0.3La, the fine needle-like phases increased rather than decreased. The obvious La-rich phase with Fe-rich phases accompaniment was detected by EDS, and these La-rich phases were mainly presented as massive and fine needles; compositionally, La maintained a high correlation with Cu, as shown in the EDS results and composition 5 of Table 2. To avoid chance, the present work continued to observe this phenomenon using the experimental results after heat treatment. It is also noteworthy that there was an aggregated distribution of the Fe-rich phase and Al<sub>2</sub>Cu, and careful observation reveals that Al<sub>2</sub>Cu grows along the surface of the Fe-rich phase. Since the lattice constant of the Fe-rich phase is very close to that of Al<sub>2</sub>Cu with a mismatch of less than 5%, it is evident that the Fe-rich phase can be a good nucleation substrate for Al<sub>2</sub>Cu [37,38].

### 3.2. As-Cast Performance Characterization

#### 3.2.1. As-Cast Mechanical Properties Testing

The results of the hardness and tensile properties tests of the six groups of samples in the as-cast state are shown in Figure 6. As shown in Figure 6a, base had the lowest hardness of  $95.6 \pm 3.8$  HV; both Al-Ti-B and 0.1La added alone improved the hardness value, reaching  $97.6 \pm 3.0$  HV and  $96.1 \pm 3.2$  HV, respectively. Similar to the microstructure size characterization, the combined addition of the two also showed better results in hardness than adding them alone. However, unlike the previous description, the performance of AlTiB + 0.3La was not the best.

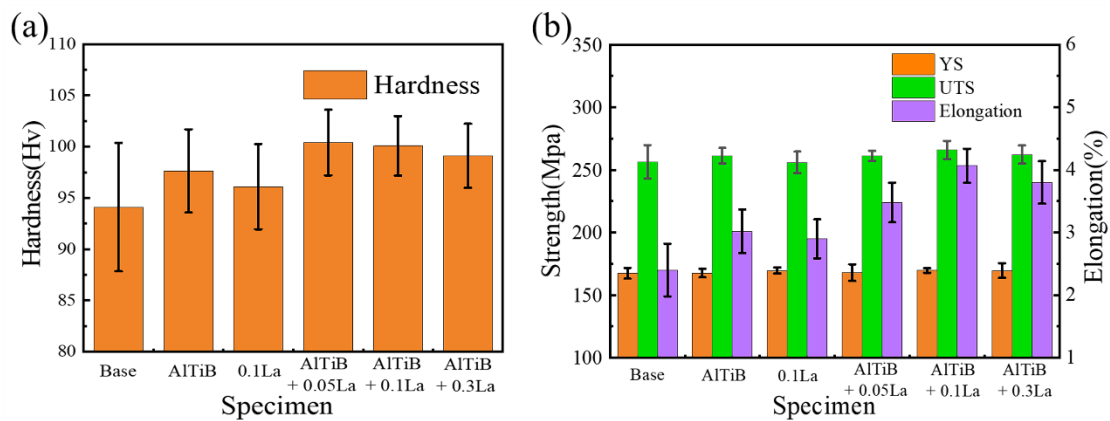


**Figure 6.** As cast mechanical properties (a) hardness test; (b) tensile properties.

In the tensile experiments of Figure 6b, six alloy samples did not show any big difference in the yield strength and tensile strength. The yield strength of the six alloy samples was concentrated at around 168 MPa, and the tensile strength was about 260 MPa. The optimization effect of the additive on the performance was mainly reflected in the elongation. Base had an elongation of  $2.4 \pm 0.4\%$ , and the addition of Al-Ti-B and 0.1La alone reduced the influence of defects on the performance to a certain extent. The elongation reached  $3.0 \pm 0.4\%$  and  $2.9 \pm 0.3\%$ , corresponding to an increase of 25.8% and 20.8%, respectively. Moreover, the composite addition of Al-Ti-B and La further enhanced the plasticity of the cast alloy, with the most obvious enhancement of AlTiB + 0.1La, whose  $4.1 \pm 0.3\%$  elongation increased by 69.6% compared to base.

### 3.2.2. As-Cast Fracture Characteristics

As shown in Figure 7, the as-cast fracture morphology of six alloys was composed of dimples, tearing ridges and a small number of cleavage planes. Specifically, the dimples of base were coarse and irregular, and large-sized holes accompanied by two obvious microcracks were found. AlTiB and 0.1La had significantly reduced micropores, and their dimples were more homogeneous than those of base, but at the same time, significant cleavage planes were found in the above two groups of samples. The last three groups of alloys exhibit good plasticity due to their fine microstructure and less  $\beta$ -Fe. They have small uniform dimples, which are ductile fractures. In addition, it is well known that the fracture of Al-Si alloys tends to start from the hard and brittle second phase, such as the Fe-rich phase and coarse eutectic Si, due to the development of internal stresses during plastic deformation. Taking the fracture of AlTiB + 0.05La as an example, one of the microcracks was observed, and its region was examined by EDS. The crack extension path was found to be very consistent with the distribution of Fe elements, so we concluded that the Fe-rich phase was one of the main causes of fracture.

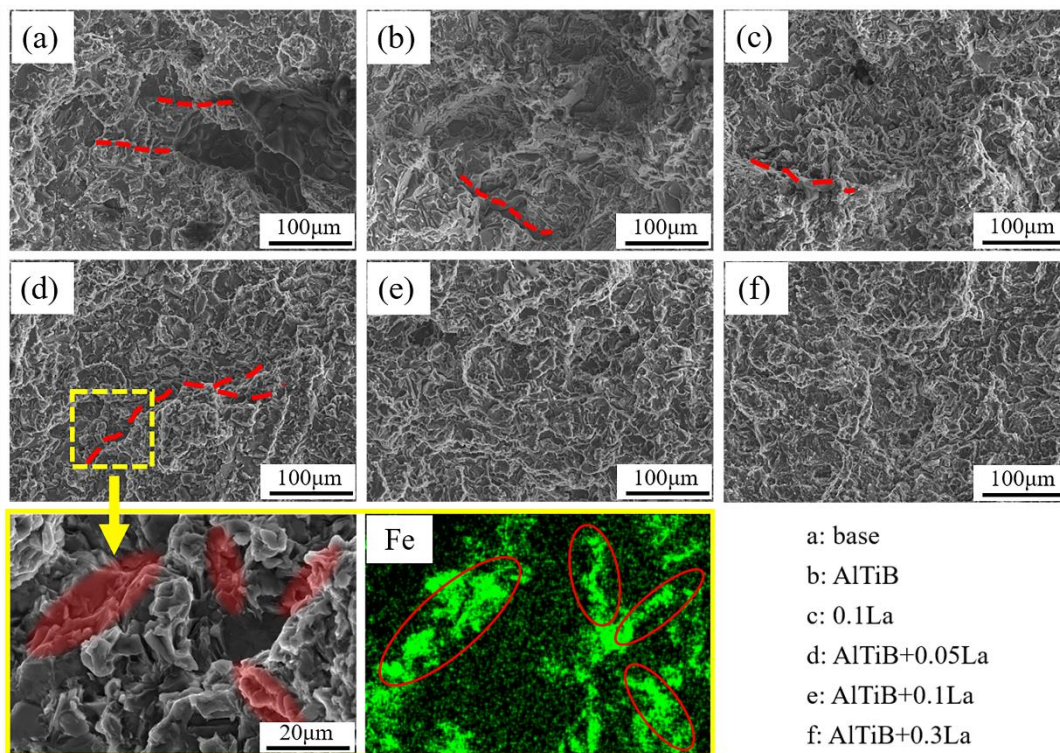


**Figure 7.** As cast typical fracture characteristics of 6 groups of alloys. (a)base, (b) AlTiB, (c) 0.1La, (d) AlTiB + 0.05La, (e) AlTiB + 0.1La, (f) AlTiB + 0.3La.

### 3.3. Microstructure Characteristics after Peak Aging

#### 3.3.1. Two-Dimensional Observation of Intermetallics after Peak Aging

The samples after heat treatment were examined by SEM/EDS. After the solid solution treatment, the low melting point eutectic phase ( $\text{Al}_2\text{Cu}$ , Q phase) dissolved into the matrix, while the Fe-rich phase was retained due to its higher melting point; therefore, theoretically, all the phases in the alloy were Fe-rich and no Cu-containing intermetallic compounds. However, the results show that there was still a relatively obvious enrichment of the Cu elements, and the distribution remained highly consistent with that of La elements and some Ti elements, as shown in Figure 8. In addition, the number of RE-rich phases increased significantly with the increase of La addition. These RE-rich phases were mainly Al-Cu-La-Ti and Al-Cu-La, which were needle-like and short rod-like in morphology, similar to the  $\beta$ -Fe morphology mentioned previously. This phenomenon was particularly evident in AlTiB + 0.3La, in which a large number of fine La-rich phases were distributed in aggregation with the Fe-rich phase, making it difficult to distinguish between the two.

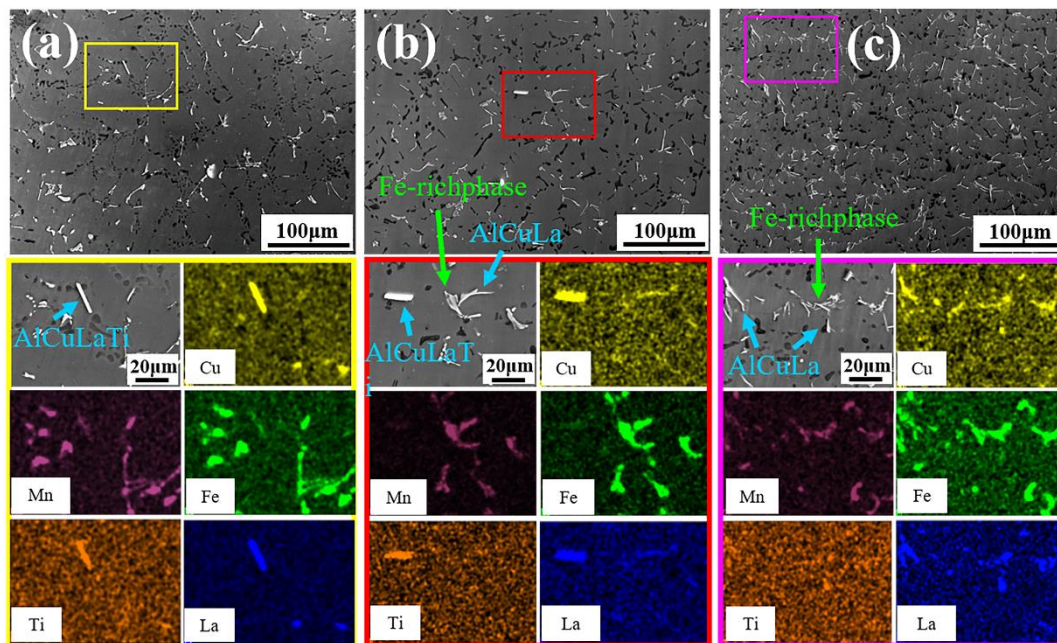


**Figure 8.** SEM/EDS microstructure images of 3 groups of alloys after peak aging: (a) AlTiB + 0.05La; (b) AlTiB + 0.1La; (c) AlTiB + 0.3La.

### 3.3.2. Three-Dimensional Characterization of Intermetallics after Peak Aging

The tomogram was obtained by X-ray tomography and imported into 3D visualization software for 3D reconstruction after the correction of artifacts, filtering and noise reduction. As the density and the atomic number increased, the absorption of X-rays by the material was enhanced, and the area on the tomogram was brighter, i.e., the gray value was greater. In this experiment, the regions with larger and brighter grayscale values were the intermetallic compounds: the two Fe-rich phases and La-rich phases, while the black regions were the micropores. Since the grayness of the Fe-rich phases and La-rich phases were similar, there was no good way to separate them, so only the intermetallic compounds and pores could be separated from the Al matrix.

The 3D morphology of the intermetallic compound of base, AlTiB, AlTiB + 0.1La after heat treatment is shown in Figure 9. Since all the Al<sub>2</sub>Cu and Q phases were dissolved after heat treatment, it was assumed that the base and AlTiB intermetallic compounds were all Fe-rich phases. Additionally, in AlTiB + 0.1La, the La-rich phase produced by the combination of La and Cu elements was also retained in the alloy. It should be noted that the 3D view will seem to have more intermetallic compounds than observed in the 2D view, which is normal. Figure 9 d e f show the intermetallic compounds of the largest size in the three groups of alloys and show that base is the largest in terms of size. The addition of Al-Ti-B and La limited the aggregation growth of intermetallic compounds, and the effect of La was more obvious, which was due to the fact that RE elements, as surface-active elements, can be adsorbed on the surface of the Fe-rich phase, hindering the diffusion of Al, Fe, Si and other elements into the Fe-rich phase and reducing the Fe-rich phase growth rate. Figure 9 g h i show the typical lamellar intermetallic compounds in the three alloys; the first two groups are  $\beta$ -Fe, and the latter group is the  $\beta$ -Fe or La-rich phase. A significant reduction in size was observed. The 3D morphology of the three lamellar structures was similar; all were very complex and had small roundness. It was speculated that the three sinuous shapes of  $\beta$ -Fe (the third group may be RE-rich phases) were formed by collisions during the growth of the lamellar structures. The shape of  $\beta$ -Fe contains “U” shaped areas, which was the result of the restriction of  $\alpha$ -Al dendrites during their growth. Similar results can be observed in Figure 5b, where intermetallic compounds (not only limited to the Fe-rich phase) grow at the dendritic gaps.

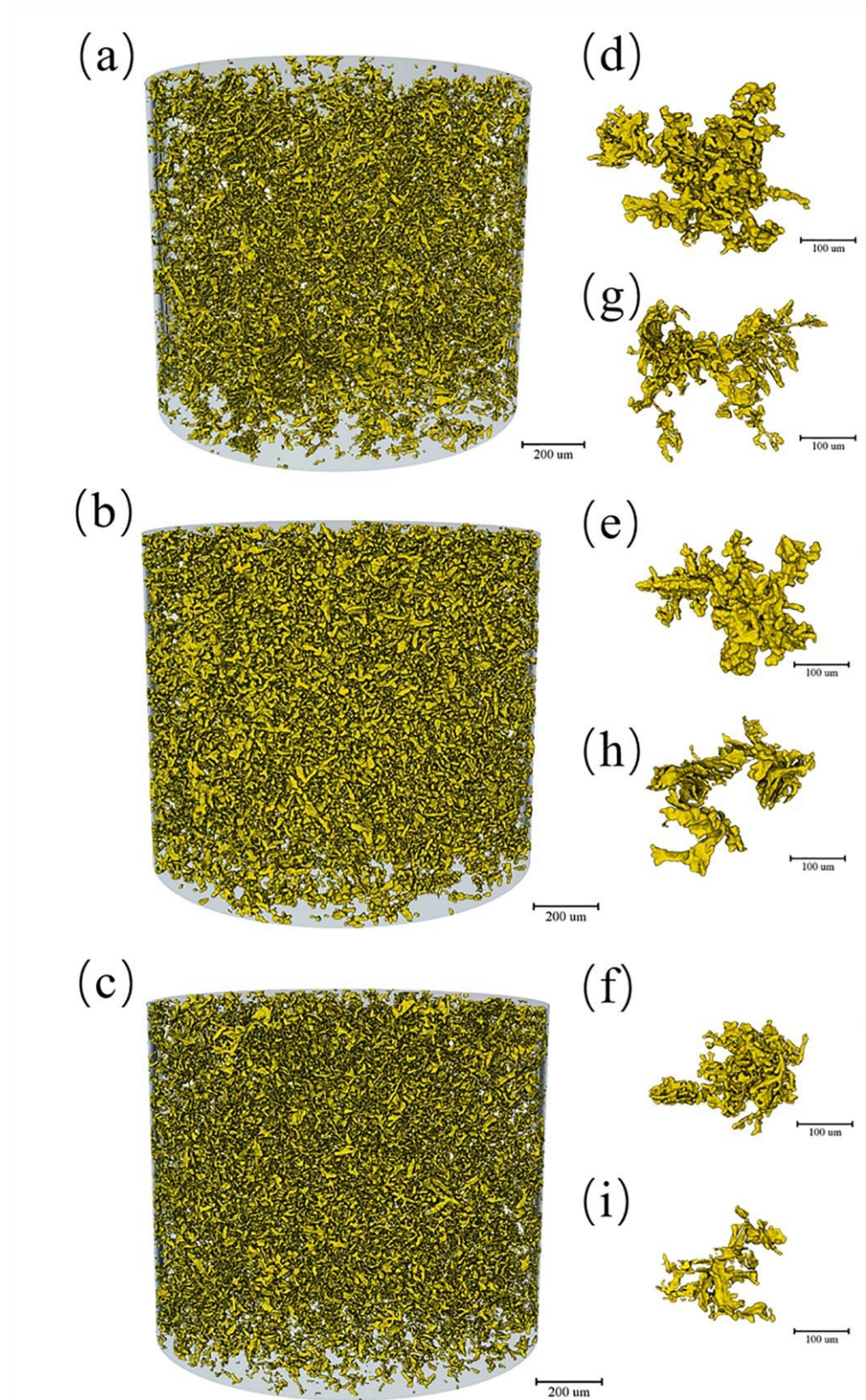


**Figure 9.** Three-Dimensional morphology and distribution characteristics of intermetallic compounds: (a) Base; (b) AlTiB; (c) AlTiB + 0.1La; (d–f) and (g–i) The largest size intermetallic compounds and typical lamellar structure corresponding to the 3 groups of alloys, respectively.

It is difficult to derive the exact variation pattern from Figure 9a–c only, so further quantitative statistics were performed on the 3D data, and the results are shown in Figure 10. Among them, Figure 10a show the average volume of particles, and it can be seen that base size is the largest, and both the refiner Al-Ti-B and La can significantly limit the intermetallic compound size; while AlTiB + 0.1La has the largest total volume of the intermetallic compound, and the percentage of large volume particles ( $>100,000 \mu\text{m}^3$ ) is the smallest among the three groups of alloys. Combined with the 2D statistical results, we can reasonably speculate that La can crush large-sized Fe-rich phases in addition to its role in converting  $\beta\text{-Fe}$  into  $\alpha\text{-Fe}$ . In addition, the depletion of Cu and Al by La elements formed La-rich phases, which also directly led to an increase in the total volume. In contrast, the addition of Al-Ti-B only limited the growth of large-size particles and had no effect on the total volume of the intermetallic compound.

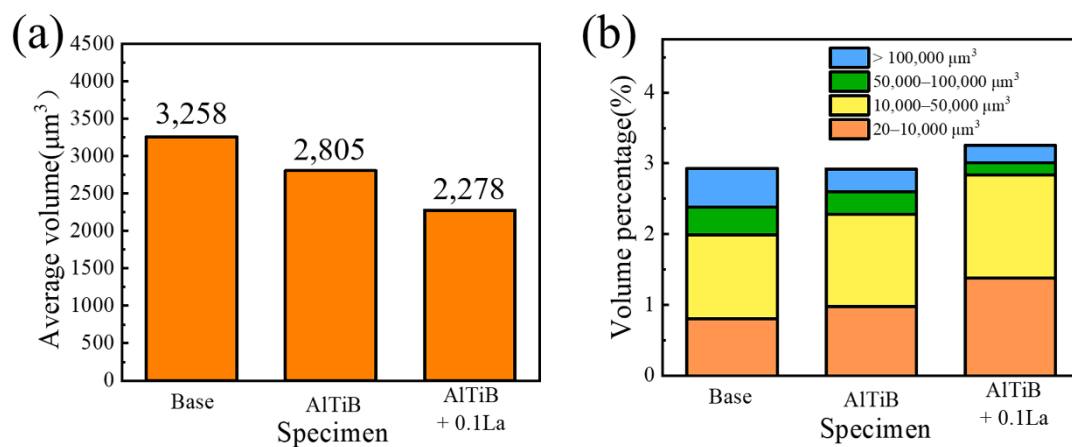


**Figure 10.** (a) Average volume of intermetallic compounds; (b) Percentage of intermetallic compounds of different sizes in the volume of the alloy.

### 3.3.3. Three-Dimensional Characterization of Microporosity after peak aging

Micropores mainly include air pores and shrinkage holes. As the temperature decreases during the casting process, the solubility of hydrogen in the Al alloy decreases, especially when the aluminum changes from a liquid phase to a solid phase, and the solubility of hydrogen decreases sharply. The hydrogen precipitated due to the poor solubility is continuously discharged to the liquid phase, resulting in a higher and higher concentration of hydrogen in the liquid phase, and when the concentration meets the requirement of stomatal nucleation, air pores begin to nucleate and grow. On the other hand, when the metal fluid cools from high temperatures, solidification shrinkage will occur. In the subsequent solidification process, shrinkage holes will be formed if no external metal fluid is replenished. From the morphology of both, the shrinkage process of shrinkage holes is influenced by dendrites and intermetallic compounds, etc., so the final shape is complex, while the air pores are more rounded because they are subjected to the pressure of hydrogen from all directions and hinder the metal liquid to the same extent [39].

Figure 11 show the 3D micropores morphology and the specific micropores with the largest size extracted from the XCT data for base, AlTiB and AlTiB+ 0.1La. It can be visualized from the 3D view that base has the largest porosity, aggregated distribution of pores and multiple large-size pores, where the largest micropores' equivalent diameter reaches  $98.8 \mu\text{m}$ . After the addition of Al-Ti-B, the aggregation distribution state of micropores did not change greatly, but the number seemed to be reduced from the overall view, and the maximum pore equivalent diameter decreased to  $78.9 \mu\text{m}$ . Additionally, the addition of 0.1% La significantly reduced the microporosity, with a maximum pore equivalent diameter of  $38.6 \mu\text{m}$ , and resulted in a very uniform overall distribution, which distinguished it from the first two groups.

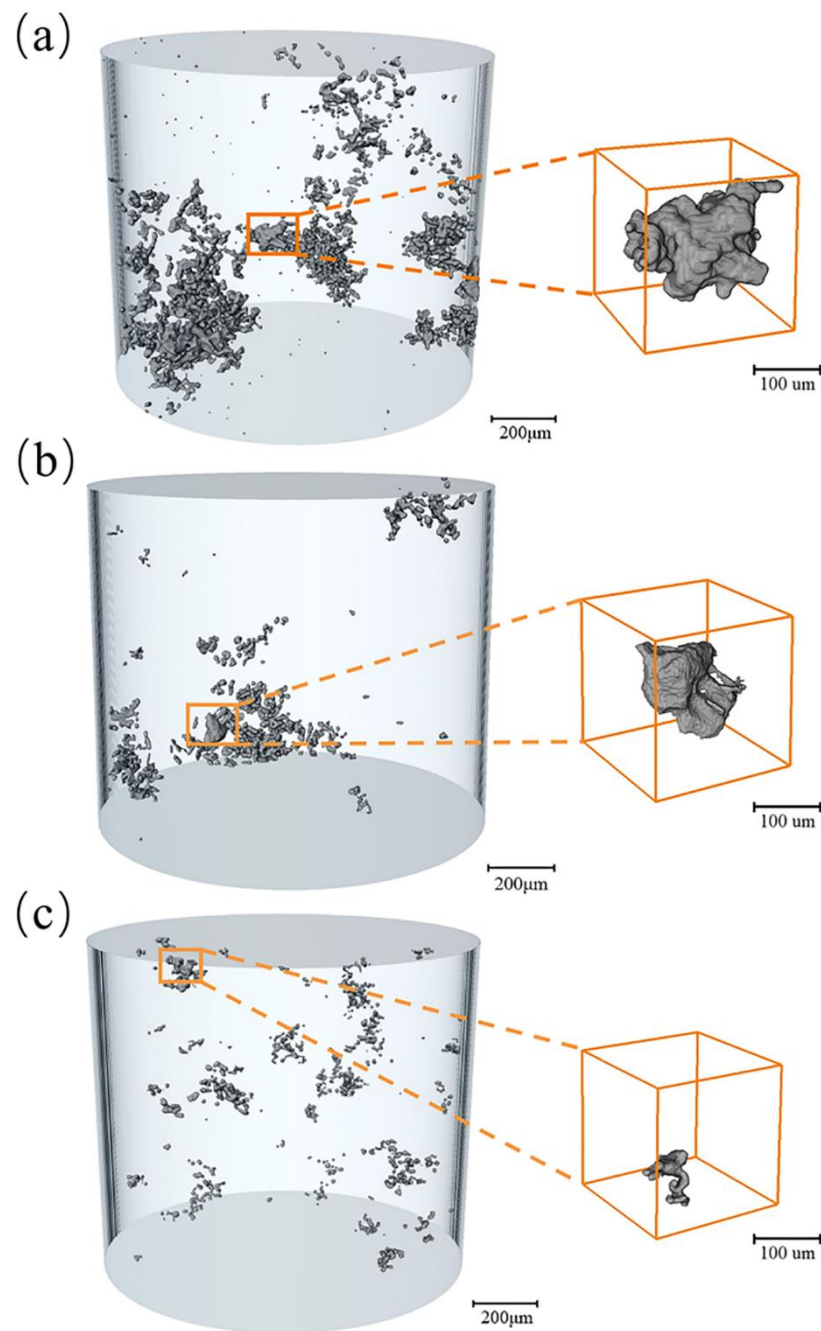


**Figure 11.** Typical pore morphology in (a) base (b) AlTiB (c) AlTiB + 0.1La and the corresponding largest size.

In addition, the morphological characteristics of the largest pores are also noteworthy. Before the addition of La, the micropores were large in size, rounded overall and presumed to be air pores. In contrast, the largest micropore of AlTiB + 0.1La had a complex and tortuous shape, consistent with the characteristics of shrinkage holes grown in the gaps of dendrites and intermetallic compounds; therefore, it was presumed to be a shrinkage hole. Consequently, we can reasonably infer that the possibility of the appearance of large-size air pores is significantly reduced due to the adsorption of H by La.

Figure 12a–c show the statistical distribution of the equivalent diameter of the micropores; Figure 12d show the average equivalent diameter and the ratio of different size micropores to the total volume. As can be seen from Figure 12, base and AlTiB have almost equal average micropore sizes, while base is larger in terms of the number of large-size

micropores and the total number of micropores. The addition of 0.1La changed the interval of microporous size concentration, resulting in most of the microporous sizes less than  $15\mu\text{m}$ . There were few large-sized micropores, with only two pores with an average equivalent diameter greater than  $25\mu\text{m}$  and none greater than  $40\mu\text{m}$ . The average equivalent diameter of AlTiB + 0.1La was  $13.6\mu\text{m}$ , compared with  $19.2\mu\text{m}$  and  $19.3\mu\text{m}$  of base and AlTiB, which was reduced by about 30.0%.

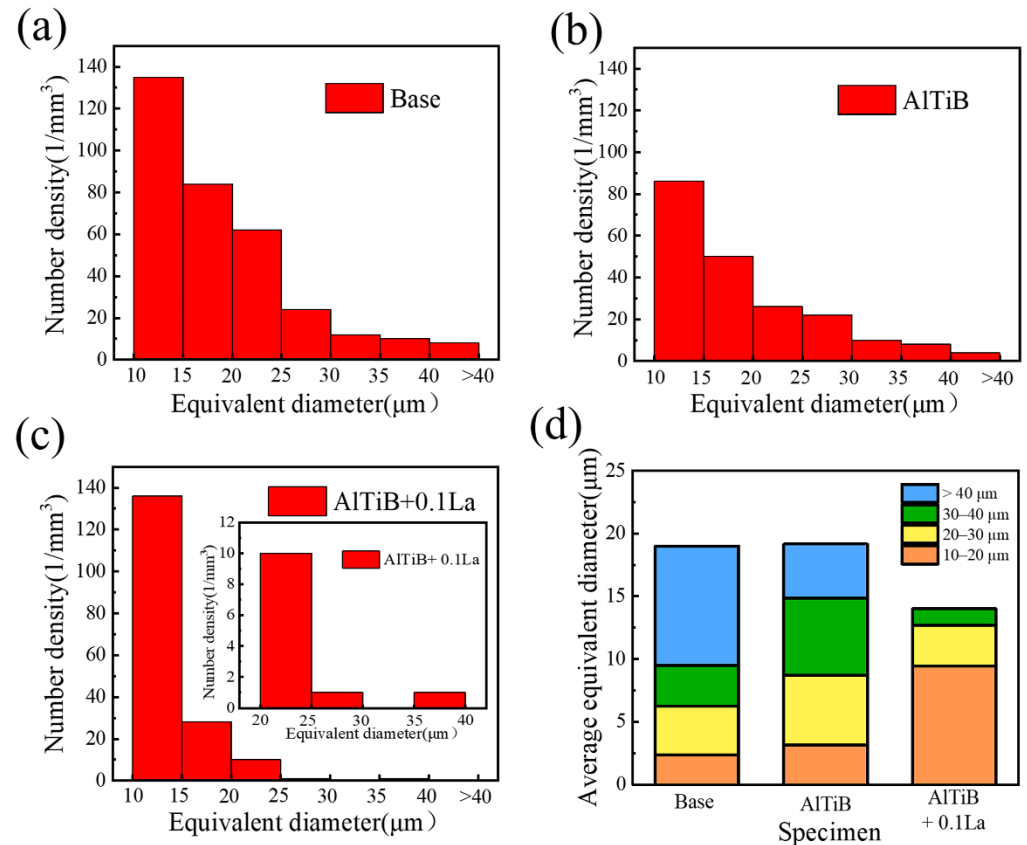


**Figure 12.** (a–c) Histogram of the equivalent diameter distribution of the morphology in the three alloys and (d) Average equivalent diameter and contribution of micropores to volume for different size ranges.

### 3.4. Mechanical Property Test after Peak Aging

Figure 13a shows the hardness values of the samples after heat treatment. Compared with the as-cast hardness test results, the heat treatment process greatly improved the alloy hardness, with all samples reaching 155.0 HV or more; but the overall variation pattern of the six groups of alloys was approximately the same compared to the as-cast state. Among the six groups of alloys, AlTiB + 0.05La had the highest value of  $161.3 \pm 2.6$  HV. However, unlike before, the hardness value of the alloy decreased rapidly with the addition of RE elements, and AlTiB + 0.3La had the worst performance with  $157.3 \pm 2.3$  HV, which was slightly lower than base and different from the as-cast test results.

The tensile test results are shown in Figure 13b, and the strength of the alloy is greatly improved compared with the results in the as-cast state. The UTS, for example, rose from 260.0 MPa in the as-cast state to more than 410.0 MPa after peak aging, with an increase of more than 58.0%; however, the elongation decreased significantly and remained at roughly 2.0%. In the cross-sectional comparison, AlTiB had the best overall performance with a yield strength of  $415.3 \pm 1.8$  MPa, a tensile strength of  $444.8 \pm 5.3$  MPa and elongation of  $2.3 \pm 0.3\%$ . The performance of 0.1La was not significantly different from that of base. Compound additions not only did not result in better mechanical properties but even had

a negative effect to some extent, both in terms of strength and plasticity. AlTiB + 0.3La performed the worst in the performance test, with a yield strength of  $399.7 \pm 2.9$  MPa, a tensile strength of  $414.6 \pm 0.4$  MPa and elongation of  $2.0 \pm 0.2\%$ . Compared to AlTiB, the decreases reached 4.0%, 6.8% and 14.3%, respectively.

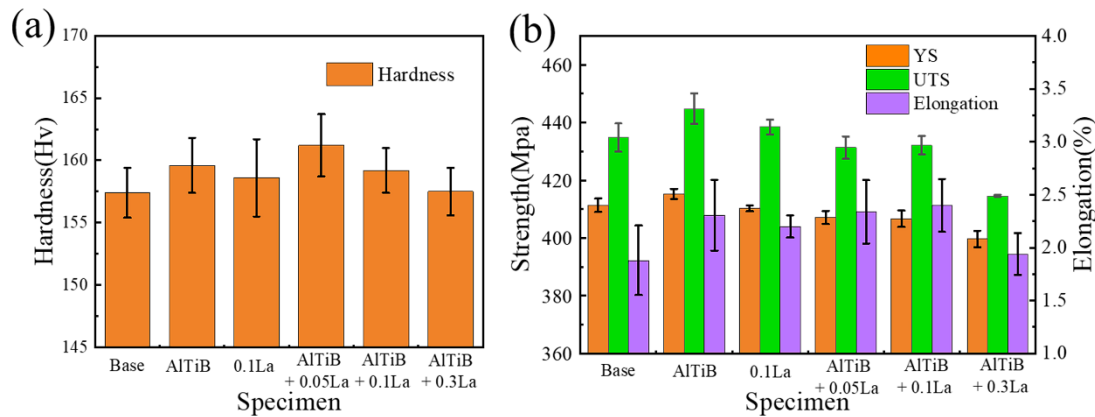


**Figure 13.** Mechanical properties after peak aging: (a) hardness test; (b) tensile properties.

## 4. Discussion

### 4.1. Effect of Al-Ti-B Addition on Microstructure and Properties

As a widely used refiner, Al-Ti-B releases intermetallic compound particles, including  $\text{Al}_3\text{Ti}$  and  $\text{TiB}_2$ , into the melt during the casting process. A large number of particles are distributed in the aluminum melt as effective heterogeneous nuclei. These nucleating particles allow the aluminum melt to start solidification at a temperature higher than the nucleation temperature, promote the formation of new grains in front of the grain growth, hinder the growth of columnar crystals from the mold wall and finally, achieve the purpose of grain refinement. In addition,  $\text{Al}_3\text{Ti}$  will dissolve in the aluminum melt to a certain extent, releasing Ti atoms. When the Ti content exceeds 0.12%, the inclusion reaction will occur at  $665^\circ\text{C}$ :  $\text{L} + \text{Al}_3\text{Ti} = \alpha\text{-Al}$ , which can also refine the grains.

As shown in Figure 3, grain refiners can also be effective in reducing SDAS. Furthermore, the fine microstructure represents a small gap between grains or dendrites, thus inhibiting the growth of second phases (eutectic Si, Fe-rich intermetallics, etc.) and micro-porosity. There is no doubt that fine microstructure size is beneficial for performance. In the case of eutectic Si, for example, the thermodynamic calculations, Figure 1b, show that the crystallization temperature of  $565.1^\circ\text{C}$  is lower than the solidification temperature of the aluminum matrix and that the fine microstructure size limits the size of the residual liquid phase zone, allowing the eutectic Si to grow with greater confinement, a conjecture confirmed by the statistical results in Figure 4.

### 4.2. Effect of Composite Addition of Al-Ti-B and La on Microstructure and Properties

In summary, the introduction of La to the W319 alloy in addition to Al-Ti-B has significant effects on the microstructure and mechanical properties, both positive and negative. For SDAS, as shown in Figure 3, both La and Al-Ti-B, which have the same refinement ability, refine the microstructure of the alloy, and the combination of the additions further enhances the refinement effect. In addition, the results show that the degree of refinement is positively correlated with the amount of La added, and more La brings a stronger optimization effect. Additionally, La has a significant effect on the densification of coarse slab eutectic Si. Although the changes before and after densification can be easily seen from the images, we also quantified the process using the extract-analysis-statistics method. As shown in Figure 4, composite addition can bring up to 29.3% improvement in the mean equivalent diameter; similar to SDAS, the more La elements in the interval 0–0.3 wt.%, the stronger the metamorphic effect. As shown in Figure 1, thermodynamic calculation

shows that the addition of the RE element La facilitates the transformation of the Fe-rich intermetallics from  $\alpha$ -Fe to  $\beta$ -Fe. Combined with the experimental characterization in Figure 5, La is enriched around the Fe-rich intermetallics and plays a role similar to that of Mn, replacing Fe atoms to a certain extent and thus reducing  $\beta$ -Fe; morphologically, the Fe-rich intermetallics change from needle to skeleton-like. La is also effective in reducing the microporosity, as can be seen in the 3D diagram. The addition of La reduces the number of micropores with an average equivalent diameter greater than 25  $\mu\text{m}$  to only two, of which none exceeds 40  $\mu\text{m}$ ; in terms of average size, the quantitative results show a reduction of about 30% in the average equivalent diameter of the micropores. Observation of the maximum pore morphology reveals that the eliminated micropores are mainly air pores, which are caused by the strong adsorption of La on H.

However, La may also bring adverse changes, especially when added in excess. Figure 1 show that the production of the La-rich phase is accompanied by a reduction of the important strengthening phase,  $\text{Al}_2\text{Cu}$ . This indicates that La depletes the Cu element to a certain extent during the casting process, resulting in a corresponding reduction of  $\text{Al}_2\text{Cu}$ . Incidentally, the production of the La-rich phase does not affect the Q phase, which also consumes Cu elements. This negative effect is more pronounced with a high amount of La addition, as Figures 5 and 8 show us the morphology in the alloy after the increase of the La-rich phase. After the heat treatment process,  $\text{Al}_2\text{Cu}$  and Q phases are fully dissolved into the matrix and precipitated by aging, which enhances the material strength. However, the presence of La in the sample inevitably reduces the effect of aging precipitation, as the remaining Cu is still retained in the La-rich phase without a solid solution, which is detrimental to the alloy properties. In addition, the advantages of Al-Ti-B and La can usually be superimposed because the refiner they have has different mechanisms to regulate alloy organization; however, in the SEM/EDS inspection (Figure 8), we found that Ti elements also react with La and Cu elements to form an  $\text{AlCuLaTi}$  phase, which is also an unfavorable phenomenon.

All the modulating behaviors are well reflected in the mechanical properties. The refinement of microstructure, the transformation of deleterious phases and reduction of microporosity under as-cast conditions ensure the properties of the alloy. As shown in Figure 6a, the addition of La enhances the hardness; however, we found that excess leads to a slight decrease in hardness, which is caused by the decrease in  $\text{Al}_2\text{Cu}$  due to the depletion of more Cu elements by La. In terms of tensile properties, Figure 6b show us that Al-Ti-B and La mainly have an effect on elongation rather than strength since microstructure size, Fe-rich intermetallics and microporosity are the main factors affecting plasticity; on the other hand, although the reduction of  $\text{Al}_2\text{Cu}$  limits the strength, the alloy is still able to maintain its original level basically. As for the heat treatment state, the negative effect is serious. As shown in Figure 13a, while 0.05 wt.% and 0.1 wt.% La can still improve or maintain the hardness of the alloy, 0.3 wt.% La offsets the full positive effect of RE because it produces an excessive amount of La-rich phase. In Figure 13b, the negative effect is more prominent, with La causing a significant decrease in strength and loss of plasticity advantage.

## 5. Conclusions

In summary, the combined effects of RE element La and Al-Ti-B grain refiners were quantitatively studied by extracting SDAS, Eutectic Si, Fe-rich intermetallics and porosity using OM, SEM and X-ray tomography. The following key conclusions can be drawn:

- (1) Both Al-Ti-B and La alone can have good refining effects, and the combined addition can boost their refining capacity, where the SDAS of the sample with Al-Ti-B + 0.3La is reduced by 39.8% compared with that of base;
- (2) La has a significant refining effect on eutectic Si, promoting the conversion of sheet eutectic Si to fibrous and granular; similarly, La can reduce the negative effects of Fe-rich intermetallics by promoting the conversion from  $\beta$ -Fe to less harmful  $\alpha$ -Fe;

- (3) While Al-Ti-B reduces the size of micropores to a certain extent by limiting their growth space, La significantly inhibits the formation of hydrogen pores in addition to limiting their growth due to the cleaning effects of absorbing H by La, which results in a reduction of the average equivalent diameter of micropores by 30.0%;
- (4) In the as-cast state, the addition of La has a limited effect on the strength, which is basically maintained at 260.0 MPa in the six groups of samples, but can significantly improve the ductility, in which the elongation of AlTiB + 0.1La refined ones increases by 69.6% as compared to base;
- (5) Since the heat treatment did not dissolve a large number of intermetallic compounds generated by the reaction of La elements with Cu and Ti, it prevented the strength from being sufficiently enhanced and offset the improvement of the alloy by La to some extent. Corresponding to the mechanical properties of the alloy, the UTS of the Al-Ti-B-refined alloy reached 444.8 MPa, while the alloy with the combined addition of Al-Ti-B + 0.3La was only 414.6 MPa, a decrease of 6.8%, and the improvement in plasticity in the as-cast state disappeared.

**Author Contributions:** Conceptualization, X.L. (Xinxu Liu) and J.W.; methodology, X.L. (Xinxu Liu) and B.W.; software, X.L. (Xinxu Liu) and C.Z.; validation, C.X., X.Y. and G.T.; formal analysis, X.L. (Xinxu Liu), Q.L. and B.W.; investigation, X.L. (Xinxu Liu), Q.L. and B.W.; resources, J.W. and H.T.; data curation, X.L. (Xinxu Liu); writing—original draft preparation, X.L. (Xinxu Liu) and B.W.; writing—review and editing, X.L. (Xiaoguang Liu) and J.W.; visualization, C.Z., C.X., X.Y., and G.T.; supervision, J.W.; project administration, J.W.; funding acquisition, J.W. and H.T. All authors have read and agreed to the published version of the manuscript.

**Funding:** The funding is supported by the National Natural Science Foundation of China-Guangxi Joint Fund (U20A20276).

**Institutional Review Board Statement:** Not applicable.

**Informed Consent Statement:** Not applicable.

**Data Availability Statement:** Not applicable.

**Acknowledgments:** The authors appreciate the tremendous help from all labmates in the Integrated Computational Materials Engineering (ICME) lab and Pengcheng Mao at the Center for Micro and Nano Technologies, Beijing Institute of Technology.

**Conflicts of Interest:** The authors declare no conflict of interest.

## References

1. Hu, X.; Jiang, F.; Ai, F.; Yan, H. Effects of rare earth Er additions on microstructure development and mechanical properties of die-cast ADC12 aluminum alloy. *J. Alloys Compd.* **2012**, *538*, 21–27. [[CrossRef](#)]
2. Yuan, W.; Liang, Z.; Zhang, C.; Wei, L. Effects of La addition on the mechanical properties and thermal-resistant properties of Al-Mg-Si-Zr alloys based on AA 6201. *Mater. Des.* **2012**, *34*, 788–792. [[CrossRef](#)]
3. Wang, W.; Pan, Q.; Lin, G.; Wang, X.; Sun, Y.; Wang, X.; Ye, J.; Sun, Y.; Yu, Y.; Jiang, F.; et al. Microstructure and properties of novel Al-Ce-Sc, Al-Ce-Y, Al-Ce-Zr and Al-Ce-Sc-Y alloy conductors processed by die casting, hot extrusion and cold drawing. *J. Mater. Sci. Technol.* **2020**, *58*, 155–170. [[CrossRef](#)]
4. Mohanty, P.; Gruzleski, J. Mechanism of grain refinement in aluminium. *Acta Met. Mater.* **1995**, *43*, 2001–2012. [[CrossRef](#)]
5. Yu, L.; Liu, X. Ti transition zone on the interface between TiC and aluminum melt and its influence on melt viscosity. *J. Mater. Process. Technol.* **2007**, *182*, 519–524. [[CrossRef](#)]
6. Ma, T.; Chen, Z.; Nie, Z.; Huang, H. Microstructure of Al-Ti-B-Er refiner and its grain refining performance. *J. Rare Earths* **2013**, *31*, 622–627. [[CrossRef](#)]
7. Maxwell, I.; Hellawell, A. A simple model for grain refinement during solidification. *Acta Met.* **1975**, *23*, 229–237. [[CrossRef](#)]
8. Yan, G.; Wenlin, C.; Zhen, G.; Liang, W. Effect of Rare Earth Metals on Mechanical and Corrosion Properties of Al-Zn-Mg-Cu-Zr Alloy. *Rare Met. Mater. Eng.* **2017**, *46*, 2070–2075. [[CrossRef](#)]
9. Colombo, M.; Gariboldi, E.; Morri, A. Influences of different Zr additions on the microstructure, room and high temperature mechanical properties of an Al-7Si-0.4Mg alloy modified with 0.25%Er. *Mater. Sci. Eng. A* **2018**, *713*, 151–160. [[CrossRef](#)]
10. Barkov, R.Y.; Prosviryakov, A.S.; Khomutov, M.G.; Pozdniakov, A.V. Effect of the Zr and Er Content on the Structure and Properties of the Al-5Si-1.3Cu-0.5Mg Alloy. *Phys. Met. Metallogr.* **2021**, *122*, 614–620. [[CrossRef](#)]

11. Barkov, R.Y.; Mochugovskiy, A.G.; Khomutov, M.G.; Pozdniakov, A.V. Effect of Zr and Er Small Additives on the Phase Composition and Mechanical Properties of Al-5Si-1.3Cu-0.5Mg Alloy. *Phys. Met. Metallogr.* **2021**, *122*, 161–168. [[CrossRef](#)]
12. Colombo, M.; Gariboldi, E.; Morri, A. Er addition to Al-Si-Mg-based casting alloy: Effects on microstructure, room and high temperature mechanical properties. *J. Alloys Compd.* **2017**, *708*, 1234–1244. [[CrossRef](#)]
13. Zhang, M.; Wang, J.; Wang, B.; Xue, C.; Liu, X. Quantifying the effects of Sc and Ag on the microstructure and mechanical properties of Al-Cu alloys. *Mater. Sci. Eng. A* **2021**, *831*, 142355. [[CrossRef](#)]
14. Zhang, Z.; Chen, K.-H.; Fang, H.-C.; Qi, X.-W.; Liu, G. Effect of Yb addition on strength and fracture toughness of Al-Zn-Mg-Cu-Zr aluminum alloy. *Trans. Nonferrous Met. Soc. China* **2008**, *18*, 1037–1042. [[CrossRef](#)]
15. Zheng, Q.; Zhang, L.; Jiang, H.; Zhao, J.; He, J. Effect mechanisms of micro-alloying element La on microstructure and mechanical properties of hypoeutectic Al-Si alloys. *J. Mater. Sci. Technol.* **2020**, *47*, 142–151. [[CrossRef](#)]
16. Mao, G.; Liu, S.; Wu, Z.; Zhu, C.; Gao, W. The effects of Y on primary  $\alpha$ -Al and precipitation of hypoeutectic Al-Si alloy. *Mater. Lett.* **2020**, *271*, 127795. [[CrossRef](#)]
17. Ahmad, R.; Asmael, M.B.A. Influence of Lanthanum on Solidification, Microstructure, and Mechanical Properties of Eutectic Al-Si Piston Alloy. *J. Mater. Eng. Perform.* **2016**, *25*, 2799–2813. [[CrossRef](#)]
18. Nogita, K.; McDonald, S.D.; Dahle, A.K. Eutectic Modification of Al-Si Alloys with Rare Earth Metals. *Mater. Trans.* **2004**, *45*, 323–326. [[CrossRef](#)]
19. Wang, J.; Lee, P.D.; Hamilton, R.W.; Li, M.; Allison, J. The kinetics of Fe-rich intermetallic formation in aluminium alloys: In situ observation. *Scr. Mater.* **2009**, *60*, 516–519. [[CrossRef](#)]
20. Taylor, J.; Schaffer, G.; Stjohn, D. The role of iron in the formation of porosity in Al-Si-Cu-Based casting alloys: Part II. A phase-diagram approach. *Metall. Mater. Trans. A Phys. Metall. Mater. Sci.* **1999**, *30*, 1651–1655. [[CrossRef](#)]
21. Murali, S.; Raman, K.S.; Murthy, K.S.S. Morphological studies on  $\beta$ -FeSiAl5 phase in Al-7-Si-0.3Mg alloy with trace additions of Be, Mn, Cr, and Co. *Mater. Charact.* **1994**, *33*, 99–112. [[CrossRef](#)]
22. Shi, Z.; Wang, Q.; Zhao, G.; Zhang, R. Effects of erbium modification on the microstructure and mechanical properties of A356 aluminum alloys. *Mater. Sci. Eng. A* **2015**, *626*, 102–107. [[CrossRef](#)]
23. Li, Z.; Yan, H. Modification of primary  $\alpha$ -Al, eutectic silicon and  $\beta$ -Al<sub>5</sub>FeSi phases in as-cast AlSi<sub>10</sub>Cu<sub>3</sub> alloys with (La+Yb) addition. *J. Rare Earths* **2015**, *33*, 995–1003. [[CrossRef](#)]
24. Dash, M.; Makhlof, M. Effect of key alloying elements on the feeding characteristics of aluminum-silicon casting alloys. *J. Light Met.* **2001**, *1*, 251–265. [[CrossRef](#)]
25. Moustafa, M.A. Effect of iron content on the formation of  $\beta$ -Al<sub>5</sub>Fe Si and porosity in Al-Si eutectic alloys. *J. Mater. Process. Technol.* **2009**, *209*, 605–610. [[CrossRef](#)]
26. Zhang, M.; Liu, K.; Wang, B.; Liang, T.; Han, J.; Wang, J. Accelerating pore nucleation and eutectic Si growth kinetics by increasing Cu and Sc for Al-Si-Mg alloys: In-situ observation. *J. Alloys Compd.* **2021**, *869*, 159173. [[CrossRef](#)]
27. Wang, B.; Zhang, M.; Wang, J. Quantifying the effects of cooling rates and alloying additions on the microporosity formation in Al alloys. *Mater. Today Commun.* **2021**, *28*, 102524. [[CrossRef](#)]
28. Liu, K.; Wang, J.; Yang, Y.; Zhou, Y. Effect of cooling rate on carbides in directionally solidified nickel-based single crystal superalloy: X-ray tomography and U-net CNN quantification. *J. Alloys Compd.* **2021**, *883*, 160723. [[CrossRef](#)]
29. Liu, K.; Wang, J.; Yang, Y.; Zhou, Y.; Yang, Y.; Cao, C. An integrated microporosity model of 3D X-ray micro-tomography and directional solidification simulations for Ni-based single crystal superalloys. *Comput. Mater. Sci.* **2021**, *188*, 110172. [[CrossRef](#)]
30. Ghassemali, E.; Riestra, M.; Bogdanoff, T.; Kumar, B.S.; Seifeddine, S. Hall-Petch equation in a hypoeutectic Al-Si cast alloy: Grain size vs. secondary dendrite arm spacing. *Procedia Eng.* **2017**, *207*, 19–24. [[CrossRef](#)]
31. Yan, K.-J.; Huang, W.-Q.; Zuo, Z.-X.; Ren, P.-R.; Li, D.-W.; Zhao, C.-Z.; Song, J.-N.; Zhang, X.-B. Microstructure based analysis and predictive modeling of cast Al7Si1.5Cu0.4Mg alloy mechanical properties. *Mater. Today Commun.* **2021**, *30*, 103102. [[CrossRef](#)]
32. Ding, W.; Zhao, X.; Chen, T.; Zhang, H.; Liu, X.; Cheng, Y.; Lei, D. Effect of rare earth Y and Al-Ti-B master alloy on the microstructure and mechanical properties of 6063 aluminum alloy. *J. Alloys Compd.* **2020**, *830*, 154685. [[CrossRef](#)]
33. Easton, M.; Stjohn, D. An analysis of the relationship between grain size, solute content, and the potency and number density of nucleant particles. *Met. Mater. Trans. A* **2005**, *36*, 1911–1920. [[CrossRef](#)]
34. Zhang, M.; Liu, K.; Han, J.; Qian, F.; Wang, J.; Guan, S. Investigating the role of Cu, Zr and V on the evolution of microstructure and properties of Al-Si-Mg cast alloys. *Mater. Today Commun.* **2021**, *26*, 102055. [[CrossRef](#)]
35. Li, J.H.; Suetsugu, S.; Tsunekawa, Y.; Schumacher, P. Refinement of Eutectic Si Phase in Al-5Si Alloys with Yb Additions. *Metall. Mater. Trans. A* **2013**, *44*, 669–681. [[CrossRef](#)]
36. Jia, K.; Yu, W.-B.; Yao, J.-M.; Zhang, S.; Wu, H. Al-9.00% Si-0.25% Mg alloys modified by ytterbium. *Rare Met.* **2017**, *36*, 95–100. [[CrossRef](#)]
37. Li, Z.; Samuel, A.M.; Samuel, F.H.; Ravindran, C.; Valtierra, S. Effect of alloying elements on the segregation and dissolution of CuAl<sub>2</sub> phase in Al-Si-Cu 319 alloys. *J. Mater. Sci.* **2003**, *38*, 1203–1218. [[CrossRef](#)]
38. Rømming, C.; Hansen, V.; Gjønnes, J. Crystal structure of  $\beta$ -Al<sub>4.5</sub>FeSi. *Acta Crystallogr. Sect. B Struct. Sci. Cryst. Eng. Mater.* **1994**, *50*, 307–312. [[CrossRef](#)]
39. Xue, C.; Zhang, Y.; Mao, P.; Liu, C.; Guo, Y.; Qian, F.; Zhang, C.; Liu, K.; Zhang, M.; Tang, S.; et al. Improving mechanical properties of wire arc additively manufactured AA2196 Al-Li alloy by controlling solidification defects. *Addit. Manuf.* **2021**, *43*, 102019. [[CrossRef](#)]